1   **Testing the applicability of standardised growth curves (SGC) for chemically**
2   **heterogeneous single-grain feldspars from the Atacama Desert, Chile**

3   Linda A.E. Maßon[1*], Svenja Riedesel[1,2], Anja Zander[1], Mariana Sontag-González[3,4], Tony
4   Reimann[1]

5   [1] Institute of Geography, University of Cologne, Germany

6   [2] Radiation Physics Division, Department of Physics, Technical University of Denmark, Denmark

7   [3] Institute of Geography, Justus-Liebig-University Gießen, Germany

8   [4] Department of Geosciences, Stony Brook University, NY 11794-2100, USA

9   * Correspondence: l.masson@uni-koeln.de

10

13

14   **Abstract**

15   The Atacama Desert is generally considered the driest non-polar desert on Earth and is therefore an ideal
16   study area for exploring the water and biota free endmember of Earth's Critical Zone (ECZ). Single
17   grain (SG) luminescence dating has successfully identified processes in the ECZ. However, SG
18   luminescence dating of Atacama Desert feldspars is challenging and time consuming since only a small
19   fraction of grains emits sufficient luminescence and their potassium (K) contents, needed for internal
20   dose rate calculations, are highly variable. Here we present an adaption of the standardised growth curve
21   (SGC) method adjusted to the conditions of Atacama Desert sediments and a correlation of single-grain
22   geochemistry and luminescence properties.

23   To evaluate if SGCs are suitable for our study site and to determine the influence of the K-content on
24   our luminescence age calculations, we used a set of five samples from the Atacama Desert and five
25   chemically and structurally different feldspar sediment extracts from various geological origins
26   worldwide. We performed a dose recovery test (DRT) using a post-infrared infrared stimulated
27   luminescence (pIRIR) protocol and measured nine major element concentrations, including K, on a
28   single grain level using a scanning electron microscope (SEM) with energy-dispersive X-ray
29   spectroscopy (EDX). The DRT dataset was then used to test the application of SGCs. The accuracy of
30   Atacama feldspar pIRIR measurements fitted onto SGCs frequently suffers from outliers in single
31   measurement cycles. We investigate the influence of calculating a synthetic regenerative signal (sR) for
32   SGC fitting, to reduce the effect of outliers on individual grain measurements. Furthermore, we reduced
33   the regenerative cycles (rc) used for our sR approach, to test if shorter protocols would result in
34   equivalent dose (D_e) estimates in agreement with longer protocols. We then calculated Spearman rank
35   correlations between the results obtained with our modified SGC and the SAR protocol, luminescence
36   signal intensities, and the geochemical dataset.

37 Finally, we present a new method of fitting data onto a SGC which significantly decreases measurement

38 time, without risking the inclusion of outliers. We furthermore show that the luminescence signal

39 intensities, the D_e values and their dose recovery ratios obtained with our SGC method and a SAR

40 protocol, are independent of the sample geochemistry.

41

1. Introduction

43 In the recent past the interrelationship of life and the evolution of Earth's surface has been subject to

44 intensified research activities (e.g., Amundson et al., 2007; Starke et al., 2020). The outermost shell of

45 our planet, in which rocks, soils, water, air and biota interact and thus where this interrelationship takes

46 place, is often referred to as the Earth's Critical Zone (ECZ) (Giardino and Houser, 2015). The Atacama

47 Desert in Chile, generally considered the driest non-polar Desert on Earth, is an ideal study site to

48 explore the dynamics of the water and biota free endmember of ECZ systems (e.g., Dietrich and Perron,

49 2006; Oeser et al., 2018; Tchakerian and Pease, 2015).

50 Single-grain luminescence dating has successfully been applied to infer sediment transport and mixing

51 processes in the ECZ in various geological settings dissimilar to the Atacama Desert (Bonnet et al.,

52 2019; Reimann et al., 2017; Román-Sánchez et al., 2019a,b). So far, optical stimulated luminescence

53 (OSL) measurements carried out in the Atacama Desert were merely designed to determine the

54 depositional age of sediments (e.g., Bartz et al., 2020a,b; Del Río et al., 2019; Diederich et al., 2020;

55 May et al., 2020, 2015; Ritter et al., 2019; Veit et al., 2015) and dynamics inside a calcium sulphate

56 wedge (Zinelabedin et al., 2022). Those studies revealed the unfavourable properties of Atacama Desert

57 sediments especially regarding quartz OSL measurements. Quartz from the Atacama Desert has been

58 shown to have a very low OSL sensitivity and unstable signal components (Bartz et al., 2020a; Del Río

59 et al., 2019; May et al., 2015; Veit et al., 2015). Furthermore, a previous study on the applicability of

60 luminescence dating of coarse grain feldspars from the Atacama Desert found highly variable potassium

61 (K) contents within each sample and merely ~ 1 % of the measured feldspar grains gave a post-infrared

62 infrared stimulated luminescence (pIRIR) signal suitable for dating (Zinelabedin et al., 2022). The

63 heterogeneity of K-contents in feldspars poses a challenge in calculating internal dose rates and raises

64 the question of whether the chemical composition of feldspars is related to luminescence properties.

65

66 Problematic quartz OSL properties have been reported previously and have been associated with the

67 quartz source area (e.g., Bartz et al., 2020a; Sawakuchi et al., 2011; Tokuyasu et al., 2010), the

68 depositional context of the sample (e.g., Fitzsimmons et al., 2010; Li and Wintle, 1992) or too few

69 reworking cycles (e.g., Sawakuchi et al., 2011; Steffen et al., 2009). In some cases, coping strategies

70 have been developed (Fuchs and Owen, 2008, Sawakuchi et al., 2011). So far, due to its unfavourable

71 OSL properties, quartz has been discarded for luminescence dating of Atacama Desert sediments (e.g.

72 Bartz et al., 2020a; Zinelabedin et al., 2022). Considerably fewer studies have addressed problematic

73 feldspars. Single-grain measurements of feldspars can be challenging and time-consuming, particularly
74 when only a small percentage of grains emits suitable luminescence signals (e.g. Brill et al., 2018;
75 O'Gorman et al., 2021; Sontag-González et al., 2021; Zinelabedin et al., 2022). In such cases many SG
76 discs have to be measured before a sufficient number of grains has been obtained to calculate a robust
77 palaeodose. This can result in such samples not being investigated further (Brill et al., 2018).
78 Establishing a standardised growth curve (SGC) for single-grain feldspar pIRIR measurements reduces
79 the measurement time considerably (Li et al., 2018). Sontag-González et al. (2021) showed that SGCs
80 are also suitable for feldspars with unfavourable luminescence properties and a complex mineralogy.

81

82 Atacama Desert feldspars studied so far show highly variable K-contents with on average low K-
83 concentrations (Zinelabedin et al., 2022). It is generally considered that a feldspar grain giving a
84 luminescence signal has a K-content in the range of 8 to 13 % (12.5 ± 0.5 % Huntley and Baril, 1997 or
85 10 ± 2 % Smedley et al., 2012). Furthermore, Prescott and Fox (1993) (thermoluminescence) and
86 Spooner (1992) (infrared stimulated luminescence) presented data for the whole composition range of
87 the feldspar mineral group, showing a positive correlation of K-contents and signal intensity. In contrary,
88 O'Gorman et al. (2021) and Zinelabedin et al. (2022) not only showed that grains with lower K-
89 concentrations may emit suitable pIRIR signals but also that the majority of grains in a sample, which
90 are used for D_e calculations, may have K-contents much below the proposed literature values (< 3 %
91 and 3.9 ± 1 % respectively). Moreover Smedley et al. (2012) found no correlation between K-content
92 and signal intensity on a single-grain level. In agreement with that Finch and Klein (1999) as well as
93 Riedesel et al. (2021) propose a different source for signal intensity levels in the blue emission by linking
94 them to Al-O-Al bridges, whereas Garcia-Guinea et al. (1999) connected signal intensity to alkali ion
95 leakages caused by prolonged heating. This raises the question of whether, in the case of Atacama Desert
96 feldspars, SG K-contents have to be determined for dose rate calculation and if correlations exist
97 between the chemical composition of the feldspars and their luminescence properties.

98 In this study we aim to establish a methodological framework for time efficient single-grain
99 luminescence-based analysis of feldspar samples from the Atacama Desert. We use a test dataset
100 consisting of ten samples, five from the Atacama Desert and five chemically and structurally different
101 feldspar sediment extracts from various geological origins from around the world. A dose recovery test
102 (pIRIR$_{175}$) is performed on 500 grains per sample and the geochemistry of 300 out of the 500 grains is
103 determined by using a scanning electron microscope (SEM) equipped with an energy-dispersive X-ray
104 spectrometer (EDX). With this dataset we test the applicability of SGCs for single-grain pIRIR
105 equivalent dose (D_e) determination of Atacama Desert feldspars, in order to reduce our measurement
106 times and we use Spearman rank correlations to investigate the influence of geochemistry on
107 luminescence properties and SGC performance.

108

2. Samples and instrumentation

2.1 Samples

Our sample suit consists of ten samples of different origin and chemical composition. Five samples (ARO-18-08-LP, CSA-1-2-2, LAGU-1-1, PAG-6-4b, PAG-6-6b) originate from the Atacama Desert. The remaining five samples originate from badlands in Canada (ABLR-1), lake sediments in Japan (HAM-5), a beach ridge in Chile ~ 1000 km south of the Atacama Desert (ISM-7), the Continental Deep Drilling (KTB) borehole in Germany (KTB-383-C) and the Mont-Blanc tunnel in Italy (MBT-I-2430). We chose the non-Atacama samples to reflect a range of chemical and structural variations of feldspar. Basic information on the samples are summarised in Table 1.

118   *Table 1: Sample description.*

Sample ID	Origin and subset affiliation	Coordinates		Grain size [μm]	Grain hole size [μm]	References
ARO-18-08 LP	Atacama Desert, Chile (A)	19°39'34.02" S	69°35'51.4" W	200 – 250	300	Zinelabedin et al., 2022
CSA-1-2-2	Atacama Desert, Chile (A)	19°36'20.17" S	70°5'52.12" W	100 – 200	200	-
LAGU-1-1	Atacama Desert, Chile (A)	21°1'59.37" S	69°47'53.00" W	100 – 250	300	-
PAG-6-4b	Atacama Desert, Chile (A)	21°32'31.7" S	69°54'47.9" W	100 – 200	250	Ritter et al., 2019
PAG-6-6b	Atacama Desert, Chile (A)	21°32'31.7" S	69°54'47.9" W	100 – 200	250	Ritter et al., 2019
ABLR-1	Badlands, Canada (X)	50°1'30.6" N	104°59'15.81" W	100 – 200	250	-
HAM-5	Lake Hamana, Japan (X)	34°45'8.65" N	137°34'22.62" E	100 – 200	250	Riedesel et al., 2021, 2019
ISM-7	Beach ridge, Chile (X)	37°1'20.28" S	73°30'43.49" W	100 – 200	250	-
KTB-383-C	KTB Borehole, Germany (X)	49°48'55" N	12°7'14" W	180 – 250	250	Guralnik et al., 2015
MBT-I-2430	Mount Blanc Tunnel, Italy (X)	45°50'07'' N	6°55'59''E	180 – 212	250	Lambert, 2018

119

5

120   Prior to luminescence measurements the samples were sieved and treated with HCl (10 %), H_2O_2 (10 %)

121   and $Na_2C_2O_4$ (0.01 N), to remove carbonates and organics and to disperse the particles, respectively.

122   Subsequently, samples were sieved again to obtain different grain size fractions (Table 1). A heavy

123   liquid density separation was used to enrich the K-rich feldspar proportion ($\rho < 2.58$ g/cm³). Sample

124   KTB-383-C feldspars were etched with HF afterwards.

125   *2.2 Luminescence*

126   For the dose recovery tests the samples were loaded into standard single-grain discs under a microscope

127   under daylight conditions, for grain hole sizes used see Table 1. A single hair was used to ensure that

128   all 100 holes per disc were filled with one grain each. Despite this, for the samples CSA-1-2-2, HAM-5

129   and KTB-383-C it was sometimes unavoidable to have several grains in one hole. Prior to the dose

130   recovery test, all mounted grains were bleached in a SOL2 solar simulator for 24 h.

131   An automated Risø TL/OSL reader (DA-20) equipped with a $^{90}Sr/^{90}Y$ beta source for irradiation,

132   delivering a dose rate of ~0.08 Gy/s, was used for all luminescence measurements. A 150 mW 830 nm

133   centred IR laser stimulated the grains, and the blue (~410 nm) was detected through a combination of

134   two 2 mm Schott BG-39 filters and a 3 mm Corning 7-59 glass filter. A dose-rate map (Lapp et al.,

135   2012), created by using radiosensitive film (GAF), showed a dose uniformity across the sample area of

136   ~4.5 %. It is thus not expected to significantly contribute to the received doses of each grain. A dose

137   recovery test (DRT, given dose = 150 Gy) was carried out employing a pIRIR protocol (Thomsen et al.,

138   2008) with a preheat of 200 °C for 60 s and a pIRIR stimulation temperature of 175 °C. The IR_{50} and

139    $pIRIR_{175}$ measurement times were 2 s and 3 s, respectively. For further details on the single-aliquot

140   regenerative-dose (SAR) DRT protocol used see Table 2.

141   *Table 2: Single-grain dose recovery test SAR measurement protocol. Heating rate for steps 2-4 and 6-8 2 °C/s.*

Step	Treatment[a]	Observation
1	Given dose D_i	
2	Preheat, 60s at 200°C	
3	IRSL, 2s at 50°C	
4	IRSL, 3s at 175°C	L_x
5	Given test dose D_t	
6	Preheat, 60s at 200°C	
7	IRSL, 2s at 50°C	
8	IRSL, 3s at 175°C	T_x
9	Return to step 1	

142   [a] given dose D_i [Gy]: 150, 0, 50, 150, 300, 500, 800, 0, 50, 150; test dose D_t [Gy]: 50

143   For signal integration the first 0.2 s minus a background of the last 0.4 s of stimulation was used. Five

144   discs à 100 grains were measured per sample.

145   All D_e estimates and SGCs were derived using the numOSL R package (Peng et al., 2018) and the least-

146   squares (LS)-normalisation approach following Li et al. (2016). A measurement error for the

147   regenerative dose signal (L_x) and the corresponding test dose signal (T_x) of 2 % was used for

148   calculations. Parameters used for growth curve fitting were: "exponential model", "not forced through

149 origin" and "using a weighted procedure". Rejection criteria for the SAR and SGC approaches were as

150 follows: test dose signal following natural dose measurement (T_n) > 3 sigma above background, relative

151 standard error (RSE) of $T_n \leq 25$ %, recycling ratio = unity ± 10 %, recuperation ≤ 10 % of the natural

152 signal, recuperation ≤ 10 % of the maximum regenerative-dose signal, figure-of-merits (FOM) ≤ 10 %

153 (Peng and Li, 2017), reduced chi square ≤ 10 %. The FOM, a measure of goodness-of-fit, is calculated

154 as follows: FOM $= \sum \left| y_i^o - y_i^f \right| / \sum y_i^f * 100$ (Balian and Eddy, 1977). D_e with a RSE above 50 % were

155 rejected after their calculation. A dose value of 150 Gy was used for SAR dataset re-normalisation in

156 the pickSARdata() function.

2.3 Geochemistry (SEM-EDX)

158 Following the luminescence measurements double-sided sticky tape, on one side attached to a glass

159 microscope slide, was placed on the top side of the SG discs. The undersides of the SG discs were lightly

160 tapped with a piezoelectric ultrasonic cleaner (vibration frequency 30 ± 3 kHz) to transfer the grains

161 onto the tape. About 80 % of the grains were extracted on average. Prior to disc removal from the tape

162 the location of the disc position holes was marked on the tape. Subsequently the grains were embedded

163 in colourless two-component epoxy resin (Araldit 2020, Huntsman), with position hole placement

164 marked on the epoxy discs. The surfaces of the epoxy discs were sanded with a 1200 SiO_2 sandpaper

165 and polished to ensure that no epoxy covers the grains.

166 The chemical composition of individual grains was determined on a Zeiss Sigma 300-VP scanning

167 electron microscope (SEM) with an energy dispersive spectroscopy (EDX) attachment. The working

168 distance was set to 8.5 mm. The aperture diameter of 60 μm and an accelerating voltage of 20 kV

169 resulted in an output count rate of ~ 45,000 cps. The chemical composition of individual feldspar grains

170 was calculated based on the nine elements O, Na, Mg, Al, Si, K, Ca, Ti and Fe through stoichiometry.

171 Three out of five discs per sample were measured for their geochemical composition. For the samples

172 ISM-7, LAGU-1-1 and MBT-I-2430 two discs were analysed.

2.4 Statistic

174 For data comparison Spearman rank correlations were used (Spearman, 1904). The results of a Spearman

175 rank correlation, the Spearman's rank correlation coefficient (r_s), can range between -1 and 1, with -1

176 being a perfect negative correlation and 1 a perfect positive correlation. The closer the r_s value is to zero,

177 the weaker the correlation. We here define correlations with r_s values between 0 and ± 0.2 as very weak,

178 between ± 0.2 and ± 0.4 weak, between ± 0.4 and ± 0.6 moderate, between ± 0.6 and ± 0.8 moderate to

179 strong and between ± 0.8 and ± 1 strong. The significance of a correlation was tested using the

180 cor.mtest() function of the corrplot() package (Wei and Simko, 2023). This test results in p-values for

181 each correlation pair. If the p-value is > 0.05, the correlation is not significant.

182 All errors given here for D_e values correspond to one standard deviation. Presented arithmetic means

183 are always given with the corresponding standard error.

184

3. Standardised growth curve (SGC) application and modification

3.1 SAR and SGC

3.1.1 Procedure

To test the applicability of the SGC approach, first the dose response properties using the standard SAR approach were assessed. For further analysis the dataset was divided into two subsets, Atacama Desert (A) and external (X) samples (cf. Table 1). For each subset A and X one SGC was calculated using the numOSL R package and the above-mentioned rejection criteria. Since the Atacama Desert samples are of main interest for this research, the SGC for subset A is hereafter called SGC. The SGC for subset X is referred to as xSGC and not used for direct comparison between SAR and SGC D_e values of dataset X. The xSGC will be used in following sections for D_e calculation of grains from dataset A (see Fig. 1). Following Li et al. (2015a) two SAR cycles are needed for the D_e calculation using an existing SGC. Besides the "natural" cycle (L_n/T_n), an additional regenerative cycle with a regenerative dose D_{r1}, and test dose signal L_{r1} and T_{r1} is required for the projection onto the existing SGC. According to Li et al. (2015a) the size of D_{r1} should be close to the expected size of the D_e. Our expected dose is 150 Gy, which equals the regenerative dose of regenerative cycle R3 or R9. Unfortunately, the L_x/T_x values of regenerative cycle R3 and R9 often showed large deviations from the fitted growth curves of up to 44 % (see Fig. 2). Consequently, we decided to use regenerative cycle R2 (50 Gy) as D_{r1}.

3.1.2 Results & discussion

When using the standard SAR approach 657 grains out of 5000 analysed grains (13.1 %) passed the rejection criteria and resulted in a D_e. Most of the grains (56.7 %) were rejected due to T_n signals below 3 σ above background. Another 15.6 % were rejected based on poorly-fitted growth curves and 11.6 % were rejected for a T_n with a RSE > 25 %. For details on rejected grains see supplement Table S1. Three additional grains were rejected due to their D_e value having a RSE > 50 %. The mean of the remaining 654 D_e values was 128 ± 36.1 Gy, which corresponds to a dose recovery ratio (DRR) of 0.85 ± 0.01. MBT-I-2430 was the sample giving the most D_e values (309 grains ≈ 47.2 %) and PAG-6-4b the one with the least (1 grain = 0.15 %).

From the Atacama Desert samples (subset A) merely 88 out of 2500 grains were accepted resulting in 87 D_e. Whereas from the external samples (subset X) 569 out of 2500 grains were accepted resulting in 567 D_e values. In each subset one sample was dominating the following results. In subset A grains from sample LAGU-1-1 make up 71.3 % of the total number of accepted grains. While in subset X 54.5 % of the accepted grains were from sample MBT-I-2430. The DRR of 0.89 ± 0.02 for subset A was slightly better than for subset X with a DRR of 0.85 ± 0.01.

217 The Atacama Desert samples are of main interest for this research, thus only D_e calculations for subset
218 A are discussed in the following sections. Since the rejection criteria for the SAR and SGC methods
219 were the same, 88 grains from subset A were used for the SGC construction and subsequent D_e
220 calculation using the constructed SGCs. The goodness-of-fit of the SGC can be evaluated using the
221 FOM. Peng and Li (2017) recommended a FOM below 10 % for SGCs. Before the LS-normalisation
222 the FOM of the SGC was 16.4 %. The LS-normalisation reduced the scatter between the grains in dataset
223 A which lead to a FOM value of 10.1 %, slightly above the recommended 10 %. The D_e calculation with
224 the SGC was possible for 87 out of 88 grains. The DRR of the remaining SGC-acquired D_e values was
225 0.84 ± 0.03.

226 In previous papers the agreement of SAR and SGC results was based on their D_e values $\pm$ their 2 σ
227 standard error (e.g., Li et al., 2015a,b; Sontag-González et al., 2021). When reporting luminescence ages
228 the 1 σ standard error is commonly used (Mahan et al., 2022). The D_e values had average RSEs of
229 ~16 %, therefore the agreement within 1 σ seems inappropriate to evaluate the differences between the
230 SAR procedure and the SGC method. Therefore, we focus on the number of grains differing less than
231 $\pm$ 10 % in their calculated D_e values (Fig. 1A) and on Spearman rank correlations.
232 For 86 grains D_e values were calculated with both methods and were used for the comparison. Of those
233 86, 41 D_e values did not differ more than $\pm$ 10 %, 37 additional had indistinguishable D_e values at 1 σ
234 and 8 additional in 2 σ. SAR and SGC results correlate with a r_s of 0.81, which can be regarded as the
235 lower limit of a strong correlation.

236 There are several reasons why the D_e values of a grain calculated with the two different methods might
237 not agree within $\pm$ 10 %. Firstly, the dataset for constructing the SGC is very small (n = 88). Secondly,
238 the fit of the SGC is not considered good due to the FOM > 10 % (Peng and Li, 2017). Thirdly, even
239 though D_{rl} was chosen to reduce the influence of outliers, some L_{rl}/T_{rl} still showed deviation from the
240 growth curve of up to 35 %. Fourthly the overall large RSE of the dataset indicates poor luminescence
241 properties.
242

243
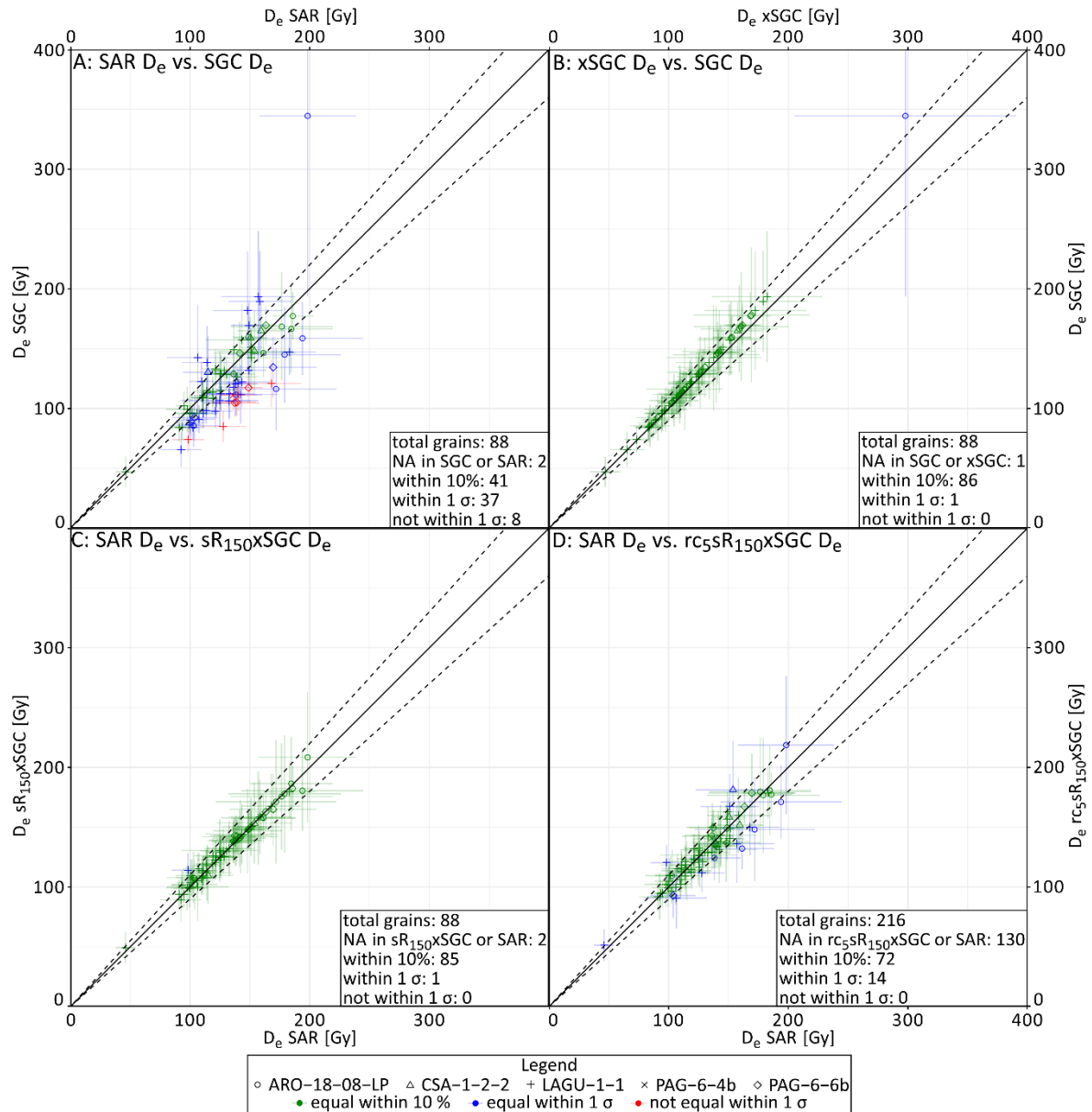
Fig. 1: evaluation of SGC performance. A) comparison of D_e from samples of dataset A (Table 1) obtained by the standard SAR procedure with D_e obtained using a SGC established with the same measurements, fitted with their L_{rI}/T_{ri} from the third SAR cycle with a D_{rI} of 50 Gy (Table 2); B) comparison of D_e from samples of dataset A obtained by a SGC, established using the same samples, and obtained by a xSGC, constructed with data from subset X (Table 1); C) comparison of D_e from samples of subset A obtained by the standard SAR procedure with D_e obtained using the xSGC from B) and fitting the individual grains with L_{sR}/T_{sR} from an synthetic cycle with a D_{rI} of 150 Gy (sR$_{150}$xSGC); D) comparison of D_e from samples of subset A obtained by the standard SAR procedure with D_e obtained using the sR$_{150}$xSGC from C) and reducing the SAR-cycles for individual growth curve fitting to the "natural" 150, 0, 50, 500, 50 Gy cycles (rc$_6$sR$_{150}$xSGC).

3.2 External SGC (xSGC)

3.2.1 Procedure

In future studies it seems more likely to use an already established SGC than constructing a SGC for every new sample side. Therefore, the established SGC might be constructed from samples with different geographical and geological origin than the samples it is used for. To mimic this scenario, we test the performance of the xSGC, build with subset X, to analyse subset A. The xSGC was constructed

10

258 in the same manner as the SGC (see section 3.1.1). For the subsequent D_e calculation of dataset A the

259 parameters of the xSGC were used in the calSGCED() function.

3.2.2 Results & discussion

261 Next the D_e results using the SGC and xSGC are compared in the same manner as SAR and SGC above

262 (Fig. 1B). Using the xSGC, D_e values for all 88 grains could be calculated. A total of 87 mutual grains

263 were used for the comparison between SGC and xSGC. All but one of them agreed within less than

264 $\pm 10\%$. If the SGC D_e is considered to be the true D_e, xSGC D_es all slightly underestimated with an

265 average of 4.14 ± 0.56 Gy. The large uncertainty is caused by one grain not being within $\pm 10\%$ in

266 unity. The correlation between both D_e results is perfect with a r_s of 1.

267 The one grain, which differed slightly more than 10 %, is still in agreement if the 1 σ errors of the two

268 D_e values are considered (cf. Fig. 1B). This particular grain had an outlier in its L_x of the second

269 regenerative cycle (R2) with an unusual low net signal and a relatively high background. SGC and xSGC

270 calculated unusually high D_e values based on this one L_x/T_x. With D_e values of 345 ± 150.8 Gy for the

271 SGC and 298 ± 92.7 Gy for the xSGC, they were around twice as high as the given dose of 150 Gy. For

272 comparison the SAR D_e for this particular grain was 198 ± 40.3 Gy, which demonstrates that outliers in

273 individual measurement cycles can have a considerable effect on the SGC results if the outliers occur in

274 the D_{r1} cycle.

275 In general, the deviation between D_e derived with the different SGCs increases with increasing L_n/T_n.

276 As with the D_e calculation using a SAR growth curve, small changes in L_n/T_n result in larger changes in

277 the D_e the closer to saturation they intersect the growth curve. L_n/T_n above $2D_0$ are therefore usually not

278 considered (Murray et al., 2002).

279 The agreement between SGC and xSGC results confirms Li et al. (2015b) findings, that a 'global SGC'

280 is suitable for feldspar samples and Mueller and Preusser (2022) observations that SGC results are not

281 biased if the same input grains are used for SGC construction and application.

282 In our future studies in the Atacama and elsewhere, the case of using a xSGC seems more likely because

283 it is created with a larger dataset and might thus be more robust. Since the correlation between SGC and

284 xSGC D_e values is perfect, all further data is generated with the xSGC.

3.3 Synthetic R (sR)

3.3.1 Procedure

287 When fitting a SAR growth curve using any function, in our case a single saturating exponential, all

288 L_x/T_x points measured are taken into account by the fit. However, when interpolating data onto a

289 constructed SGC only the natural signal and one regenerative dose point is used (Li et al., 2015a),

290 however, as mentioned in section 3.2.2 this can lead to erroneous results, should this value deviate

291 significantly from the fitted growth curve (cf. Fig. 2). Here we introduce a new parameter and procedure

292 for the projection of multiple L_x/T_x onto the constructed SGC. Instead of using a single L_x/T_x point as

293   L_{r1}/T_{r1} we chose a L_x/T_x point, which we extracted from the fitted growth curve. We term this point

294   synthetic regenerative dose (sR). For this we used the growth curves of each grain and reversed the

295   process of D_e estimation from a growth curve. We chose an sR, for example 200 Gy (cf. Fig. 2), and

296   inserted it into our exponential function (eq. 1). Thereby we projected the sR onto the growth curve

297   whereby we calculated the point of interception with the growth curve to get the value on the y-axis of

298   our synthetic L_{sR}/T_{sR} (Fig. 2).

299           $$\text{(eq. 1)} \quad \frac{L_{sR}}{T_{sR}} = a*\left(1 - exp^{(-sR*b)}\right) + c$$

300   With a, b and c being the parameters a, b and c from the grain-wise exponential growth curve, calculated

301   during the normal SAR procedure and sR a value in Gy.

302
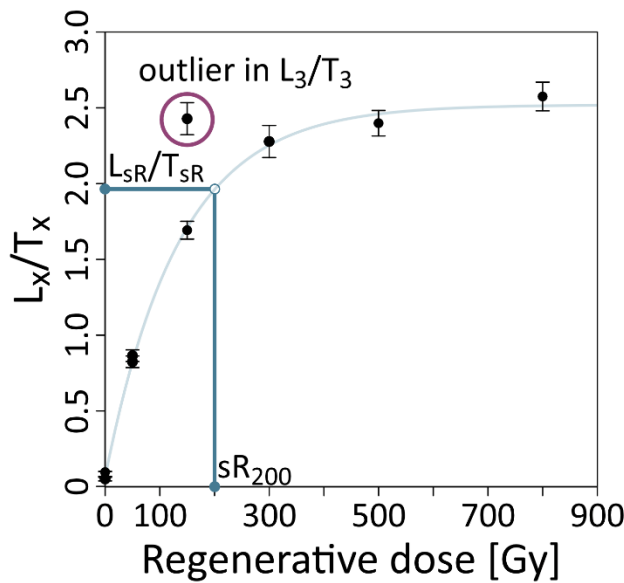
Fig. 2: Process of L_{sR}/T_{sR} determination with an sR of 200 Gy on an example exponential SG growth curve with an outlier in the L_x/T_x of the third regenerative SAR cycle ($D_i = 150$ Gy). The vertical line from the X-axes towards the growth curve illustrate the process of calculating the interception. The horizontal line from the growth curve towards the Y-axes illustrate the subsequent determination of L_{sR}/T_{sR}.

307   To evaluate if there is an influence of the size of sR on the resulting D_e and DRR we tested eight different

308   sR values: sR_{50}, sR_{100}, sR_{125}, sR_{150}, sR_{175}, sR_{200}, sR_{300} and sR_{800}, with the subscript being the size in Gy.

309   *3.3.2 Results & discussion*

310   The results were evaluated in the same manner as SAR and SGC in section 3.1.1 based on a comparison

311   of D_e and DRR results of the SAR procedure and the sR_{50-800}xSGC procedures. For detailed results of

312   all sR tested see supplement Table S2). For all sR sizes, except for 800 Gy, 86 D_e values for the 88 not

313   rejected grains were calculated. With sR_{800} 87 D_e values were calculated. Since sR_{100}, sR_{125} and sR_{150}

314   had the most grains within 10 % in unity with the SAR results, the other five sR values will not be

315   discussed further. With sR_{125} all grains had D_e values within 10 % in unity with the SAR D_e values,

316   whereas sR_{150} had one and sR_{100} three grains not within 10 %. With DRRs of 0.86 ±0.02, 0.87 ±0.02 and

317   0.89 ±0.02 for sR_{100}, sR_{125} and sR_{150} respectively all three sR procedures showed an improved DRR

318   compared to the above presented conventional SGC approach (0.84 ±0.03). The correlation between the

319   SAR D_e values and those achieved with sR_{100}, sR_{125} and sR_{150} was strong positive with Spearman's rank

320   correlation coefficient (r_s) of 0.99 for all three sR values tested. The differences between sR_{100}, sR_{125}

321   and sR_{150} were small, with sR_{125} having the most D_e results equal within 10 % with the SAR procedure

322   but sR_{150} yielding the better DRRs.

323   Deviations of sR from the expected D_e (here 150 Gy) of ~ 30 % (± 50 Gy), do not cause major alterations

324   in the D_e results in this data set. All sR ranging from 100 to 200 Gy have a strong positive correlation

325   with the SAR procedure, with a minimum r_s of 0.94. In comparison with the SAR data, if the sR was

326   slightly smaller than the expected D_e ($sR_{100,125}$), the method yielded better results than if the sR was

327   slightly larger ($sR_{175,200}$). A cause for the better agreement with the SAR results might be the overall

328   underestimation of the D_e with the SAR procedure. Since the differences between the best performing

329   sR were very small and the sR_{150} had the same DRR as the SAR procedure, we chose an sR of 150 Gy

330   for our further analysis (see Fig. 1C). Furthermore, the sR_{150} equals the recommended size for a D_{r1}(Li

331   et al., 2015a). We therefore conclude that sR should be chosen to be the same size as the expected D_e.

332   Nevertheless, considering that the D_e is normally unknown before measurement, it is reassuring that

333   choosing an sR value within 30 % of the natural dose does not seem to have too great of an effect on

334   final De calculations.

335   *3.4 Reduction of SAR cycles (rc)*

336   *3.4.1 Procedure*

337   Whilst the sR approach helps in making the interpolation onto the SGC more robust, it still requires the

338   construction of a full growth curve for every grain and thus not saving any measurement time. Here we

339   test which cycles can be removed to save time while still yielding robust D_e values with the sR_{150}xSGC

340   method. We carried out ten different reduced cycle (rc) scenarios, all containing the "natural" cycle and

341   a zero-dose cycle (recuperation). Besides these two cycles, we tested if two additional cycles are enough

342   to incorporate the sR method or if a third cycle, a recycling point, is needed as well. We also investigated

343   which dose size yielded the best results. For the recycling point we could only test 50 Gy and 150 Gy

344   since those were the only recycling doses in our SAR protocol. The ten tested rc scenarios are listed in

345   Table 3 and afterwards abbreviated with their test number according to Table 3 as a subscript. The

346   dataset used for xSGC calculation was not reduced.

347

348

349 *Table 3: reduced cycle scenarios tested for subset A. For all cycles measured see Table 2.*

Abbreviation	Used cycles	D_i of used cycles [Gy]
rc_1	N + R1 + R2 + R4	150 + 0 + 50 + 300
rc_2	N + R1 + R2 + R5	150 + 0 + 50 + 500
rc_3	N + R1 + R2 + R6	150 + 0 + 50 + 800
rc_4	N + R1 + R2 + R3 + R8	150 + 0 + 50 + 150 + 50
rc_5	N + R1 + R2 + R4 + R8	150 + 0 + 50 + 300 + 50
rc_6	N + R1 + R2 + R5 + R8	150 + 0 + 50 + 500 + 50
rc_7	N + R1 + R2 + R6 + R8	150 + 0 + 50 + 800 + 50
rc_8	N + R1 + R3 + R4 + R9	150 + 0 + 150 + 300 + 150
rc_9	N + R1 + R3 + R5 + R9	150 + 0 + 150 + 500 + 150
rc_{10}	N + R1 + R3 + R6 + R9	150 + 0 + 150 + 800 + 150

350

351 *3.4.2 Results & discussion*

352 The reduction of used SAR cycles led to an increase of accepted grains. Fewer grains were rejected due
353 to poor growth curve fitting. For detailed rejection criteria and results of all tested rc see supplement
354 Table S3 and S4.

355 The growth curves produced in rc_4 used for the sR method are not reliable since the highest given dose
356 used for their calculation is still in the linear part of the growth curves constructed with the full set of
357 SAR cycles. Many grains were falsely excluded as they appeared to be saturated. Furthermore, the
358 results did not agree well with the SAR procedure and a poor DRR was obtained (see Table S4), thus
359 rc_4 is not discussed further. All other tested rc were able to calculate ~ 200 D_e values out of the 2500
360 measured grains.
361 In a direct comparison to the SAR D_e values, all ten tested rc had at least 85 common grains with the
362 SAR results. Rc_5 had the most D_e values equal with the SAR D_e within ± 10 % and no D_e not within 1 σ.
363 Rc_1, rc_2 and rc_6 performed slightly worse, but their D_e values also did not differ more than 1 σ. The
364 remaining six rc had at least one grain, which was not within 1 σ of the SAR results and are therefore
365 not discussed further. Since the Spearman's rank correlation coefficients between rc-achieved D_e values
366 and those calculated with the SAR procedure for rc_1 and rc_2 were below the r_s of 0.94 from rc_5 and rc_6,
367 we concentrate on the latter two.

368 Rc_5 and rc_6 had the same setup for the cycle reduction, with remaining cycles being the "natural" cycle,
369 a zero-dose cycle, a recovery dose of 50 Gy plus one additional dose. The additional doses of 300 and
370 500 Gy, respectively, are between D_0 (284 Gy) and $2D_0$ (568 Gy) of the xSGC. Rc_6 was able to calculate
371 eight D_e more than rc_5 but rc_5 had the best overall results. With rc_5 197 D_e values were calculated, of
372 which 72 were equal with the SAR results within ± 10 % and the remaining 14 D_e were identical within

373   the 1 σ error (cf. Fig. 1D). The mean difference between the D_e values was 7.40 ± 0.70 Gy and the DRR

374   of rc_5 was 0.9 ± 0.02, which is slightly better than the SAR-achieved DRR of 0.89 ± 0.02.

375   Compared to the correlation of the $sR_{150}xSGC$ results, with a r_s of 0.99, the correlation of the

376    $rc_5sR_{150}xSGC$ and the SAR approach is worse with a r_s of 0.94. Nevertheless, the $rc_5sR_{150}xSGC$ is still

377   an improvement compared to the conventional SGC approach ($r_s = 0.81$, DRR $= 0.84 \pm 0.03$).

378   Furthermore, it is possible to estimate more than twice as many D_e, resulting in fewer discs to be

379   measured. The reduction of measurement cycles saves approximately 60 % of measurement time per

380   disc.

381   We therefore recommend applying the rcsRxSGC approach when dealing with problematic single grain

382   feldspars, with an sR in the size of the expected D_e and a rc scenario with a recuperation point, a

383   recycling point - smaller than the expected D_e, and an additional dose point with a size of D_0 to $2D_0$ of

384   the SGC used.

385   *3.5 Dose recovery ratio (DRR)*

386   Since our dataset is based on a dose recovery test, another measure to test the performance of our

387   approach is the dose recovery ratio. Overall the given dose of 150 Gy is underestimated by all applied

388   methods, including the standard SAR procedure. Fig. 3 shows a comparison of the D_e results achieved

389   with the SAR procedure and the $rc_5sR_{150}xSGC$ method. With the SAR procedure, 30 out of 87 grains

390   yield a DRR within the desired 1 ± 0.1. An additional 22 were still within 1 ± 0.1 if their 1 σ errors were

391   considered and 35 differed more than ± 0.1 from a DRR of 1 even when their 1 σ errors were considered.

392   Out of the 216 calculated D_e with the $rc_5sR_{150}xSGC$ method, 54 had a DRR of 1 ± 0.1. An additional 80

393   were still within 1 ± 0.1 if their 1 σ errors were considered and 82 differed more than ± 0.1 from a DRR

394   of 1 even when their 1 σ errors were considered. Thus, using the $rc_5sR_{150}xSGC$ method we observed

395   overall improved DRR.

396   The generally observed underestimation of the given dose could be due to the protocol not being suitable

397   for all samples, or due to fading of the pIRIR signals. We also considered changes in sensitivity during

398   the first measurement cycle (see Kars et al., 2014), but we could not find any indication for this (data

399   not shown).
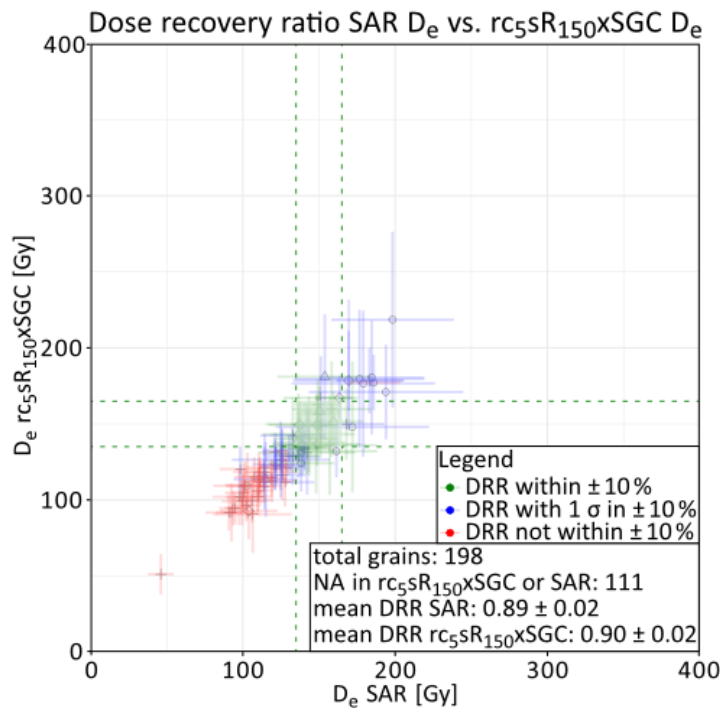
Fig.: 3: DRR from grains of subset A, calculated with the standard SAR procedure (x-axes) and the $rc_5sR_{150}xSGC$ method (y-axes). Colours of the horizontal and vertical 1 σ error bars represent if the DRR calculated with SAR or $rc_5sR_{150}xSGC$ respectively are within 1 ± 10 % (green), within 1 ± 10 % if the 1 σ error is considered (blue) or if they are not within 1 ± 10 %. Shape of the datapoints indicate the sample allocation (cf. legend Fig. 2).

4. Single grain geochemistry (SEM-EDX)

4.1 Procedure

The SEM-EDX measurements were carried out at the Institute of Geology and Mineralogy of the University of Cologne, by defining regions of interests on the grain surfaces. The elemental analysis results of each measured region were assigned to the individual grains on the basis of the tomograms of the measurements.

Unfortunately, SEM-EDX data could not be obtained for every grain. Some grains got lost during the transfer process from the discs to the tape, the position of others was slightly altered during embedding them in epoxy. If a grain was subsequently not clearly identifiable, its SEM-EDX results were not considered. For some grain positions (i.e., holes in the discs) more than one SEM-EDX result was obtained. This was either due to multiple grains being located in one hole or due to breaking of the grains during the transfer process. For grains and holes with more than one SEM-EDX measurement result, the average was calculated.

4.2 Results

The results for the nine analysed elements are summarised in Fig. 4, for detailed measurement results see supplement Table S5. 2328 grains, out of the 5000 grains analysed for their luminescence

422 characteristics, could be clearly identified on the SEM-EDX tomograms. From those 2328 grains, 250

423 gave suitable luminescence signals for D_e calculation with the SAR procedure and 492 with the

424 $rc_5sR_{150}xSGC$ method. Those grains are hereafter called luminescent grains. All luminescent grains from

425 subset A (n = 65) contained O, Na, Al, Si and K, implying that no luminescent grain from the Atacama

426 Desert was pure orthoclase. About half of them also contained Ca and Fe. From subset X (n = 434) most

427 of the grains (>400) were also composed of O, Na, Al, Si and K, with 200 of them also having Ca and

428 15 of them being pure orthoclase, based on their geochemical composition.

429
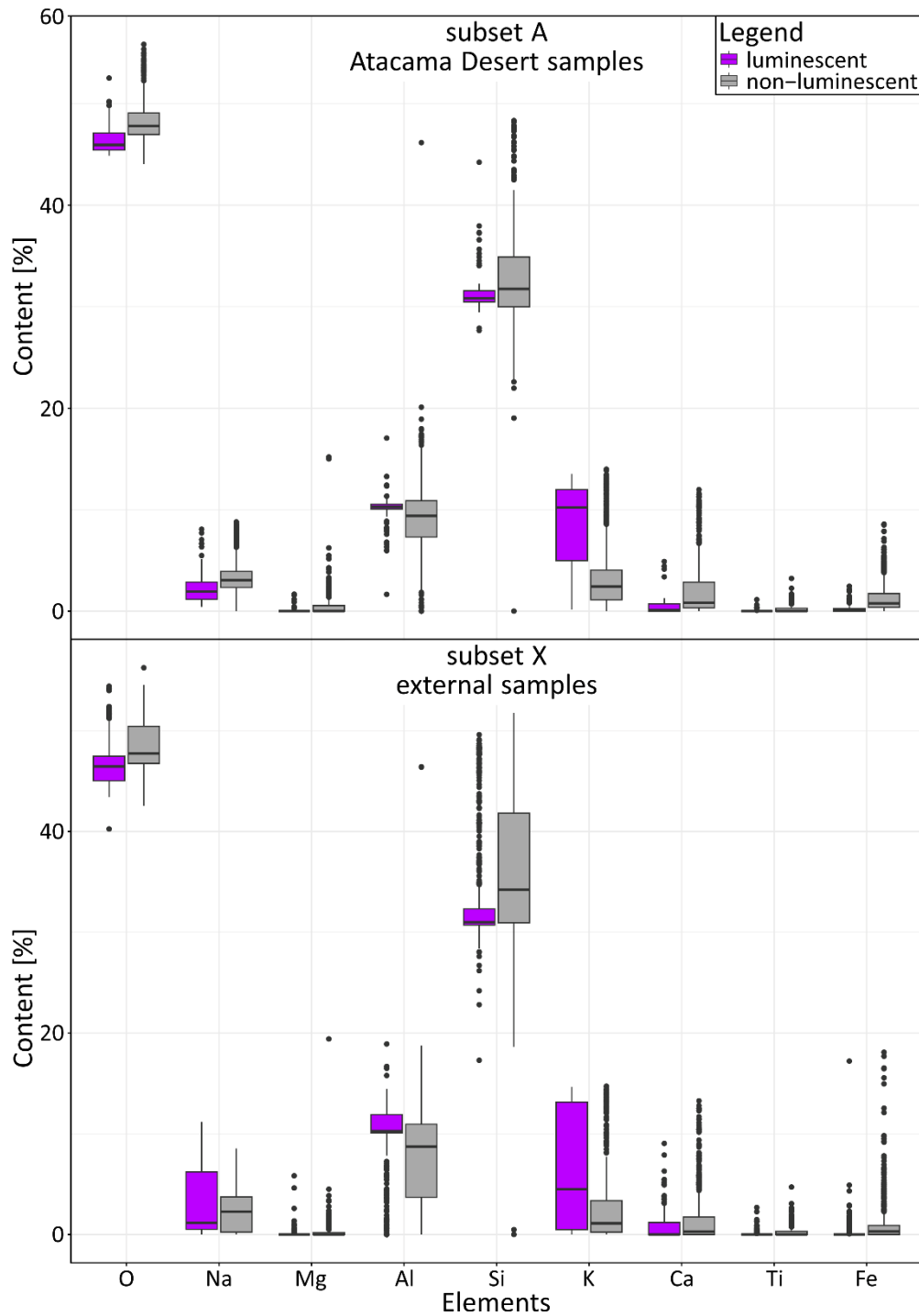
Figure 4: statistical distribution of all measured element concentrations for A) the grains from subset A and B) the grains from subset X grouped into luminescent (purple) and non-luminescent grains (gray).

The K-content of all luminescent grains varied between 0.06 wt% and 14.6 wt%, with a mean value of 7.04 ± 0.26 wt%. The coefficient of variation of all luminescent grains of 80 % indicates that luminescent grains can have a wide range of K-contents, supporting the findings from O'Gorman et al. (2021) and Zinelabedin et al. (2022).

The SEM-EDX results presented in Fig. 4 suggest that there is no clear difference between the

18

437   geochemical composition of luminescent and non-luminescent grains, neither for subset A nor subset
438   X.

439

5. Correlation of luminescence characteristics and geochemistry

441   To evaluate whether signal intensity and K-content are linked and if there are further relationships within
442   and between geochemistry and luminescence properties, we created the following nine correlation
443   matrices. We performed Spearman rank correlations for the entire dataset and the two subsets. We then
444   calculated six correlation matrices for these three categories by dividing them in luminescent and non-
445   luminescent subgroups. In addition to the nine elements from the SEM-EDX analysis, the following
446   luminescence properties were used as input variables: D_e and DRR determined with SAR, D_e and DRR
447   determined by $rc_5sR_{150}xSGC$, L_n and T_n. For better readability, only the correlation matrix of the entire
448   data set is shown in Fig. 5. The eight remaining correlation matrices can be found in supplement Fig.
449   S1.
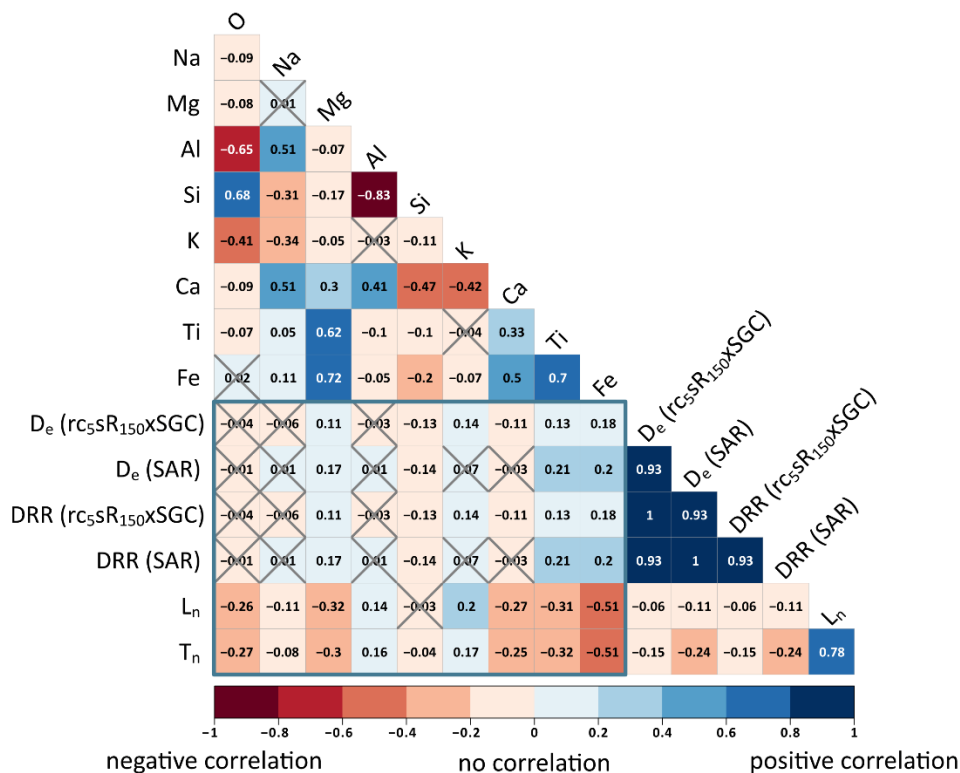
Fig. 5: correlation matrix of the complete dataset (subset A + X). Numbers in the squares represent Spearman's rank correlation coefficient values and their colour the strength of the correlation. For not significant correlations with a p-value above 0.05 % the squares are x-ed out. The turquoise square surrounds the correlation between the geochemical data and the luminescence characteristics.

455   There was no strong or moderate to strong correlation between any element and luminescence
456   characteristics if the entire dataset is considered, as can be seen inside the blue square in Fig. 5. This
457   also holds true regardless of whether the subset data or subgroups of the entire or subset data are
458   considered. Furthermore, ~ 47 % of those correlations have a p-value > 0.05 and are therefore not

459   considered significant. The most significant correlation between SEM-EDX results and luminescence is
460   the negative correlation observed between the Fe-content and the signal intensity (L_n and T_n) in the
461   correlation matrix of all grains from subset X with a r_s of -0.57 and -0.56 for L_n and T_n respectively. The
462   correlation between Fe-content and signal intensities in subset A is also negative but only very weak or
463   weak, if significant at all. There is no significant correlation between K-content and the signal intensity
464   (L_n and T_n) in subset A when only the luminescent grains are considered, but a weak negative correlation
465   can be found in subset X. In contrast, the same correlation for the non-luminescent grains is very weak
466   to weak positive in both datasets. In Fig. 5 these correlations between K-content and L_n respectively T_n
467   are weak and very weak positive, since a greater number of non-luminescent grains contribute to the
468   overall correlation in Fig. 5 (cf. Table S5). Conversely, Na and Ca contents show a positive correlation
469   with the signal intensity in the luminescent grains and a negative correlation in the non-luminescent
470   ones.

471   Within the luminescence characteristics there is no strong significant correlation between the signal
472   intensity and the D_e or the DRR. Since the D_e values and DRRs determined with the same method have
473   a perfect correlation, all correlations between D_es and DRRs determined with different methods yield
474   the same r_s values within each correlation matrix. For subset A the r_s of these correlations is 0.94, for
475   subset X and for both subsets combined it is 0.93. The correlation between L_n and T_n is almost perfectly
476   positive if only the luminescent grains are considered, but substantially weaker if all or just non-
477   luminescent grains are correlated.

478   Within the geochemical data the correlation values between the nine correlation matrices vary to a
479   greater extent than within the luminescence characteristics. Correlations found between different
480   elements reflect the general chemical characteristics of the feldspar mineral group, with Si:Al ratios
481   differing between alkali feldspars and plagioclase and with a known miscibility gap between K- and Ca-
482   feldspars. The strong negative correlation between Si and Al contents is particularly pronounced when
483   only the non-luminescent grains are considered, but visible in all nine matrices. When only the
484   luminescent grains are considered the correlations between K and Na as well as K and Ca contents are
485   moderate to strong negative, while the correlations between Na and Ca contents are moderate or very
486   strong positive. None of the K-, Na- and Ca-content correlations is more than moderate in the non-
487   luminescent correlation matrices but all are in the same directions as in the luminescent grains.

488

489   The luminescent grains from sample ARO-18-08-LP have a very strong negative correlation of -0.83
490   and -0.86 between their Fe-contents and the signal intensities L_n and T_n. Zinelabedin et al. (2022),
491   investigating the same samples, suspected that the high Fe-contents might be caused by Fe-rich coatings
492   of the feldspar grains. These iron layers around the sediment grains could on the one hand explain the
493   high Fe-content of up to 8.8 % in luminescent grains and on the other hand the observed low
494   luminescence intensities, since Fe coatings could cause absorption of the emitted luminescence (Kook

495 et al., 2011). Geake et al. (1972) and Finch and Klein (1999) present alternative explanations for the
496 negative correlation between Fe-content and L_n and T_n intensities. Ultimately, we cannot give a
497 satisfactory explanation of the observed negative correlation between Fe-content and luminescence
498 intensity at this stage.

499 The previously reported and generally accepted relationship of K-content and luminescence signal
500 intensity is not supported by our data. The non-existing correlation between K-content and signal
501 intensity in subset A confirms the findings of O'Gorman et al. (2021) and thereby falsifies the common
502 hypothesis of a positive correlation (e.g., Huntley and Baril, 1997; Prescott and Fox, 1993; Spooner,
503 1992) at least for our set of samples. The weak negative correlation in subset X is further evidence that
504 a higher K-content is not the main determinant for a high signal intensity.

505

506 **6. Conclusion**

507 Atacama Deserts feldspars are challenging for single grain luminescence measurements for two reasons:
508 firstly, only a small percentage of grains emits satisfactory luminescence signals (Ø 3.52 %) and
509 secondly their geochemical compositions are highly variable (Ø 3.40 wt% K).

510 To obtain a sufficient number of accepted grains for palaeodose calculation, numerous discs have to be
511 measured, resulting in a long overall measurement time. We therefore tested the application of the
512 standardised growth curve (SGC) method (Li et al., 2015b) with a dose recovery test using a pIRIR$_{175}$
513 protocol on ten chemically different feldspar sediment extracts. With a perfect correlation between SGC
514 and xSGC results, we confirmed, that the geographical and geological origin of the samples, for which
515 the D_e is estimated, can differ significantly from the geographical and geological origin of the samples
516 used for SGC construction and that the SGC is not biased if the same input grains are used for SGC
517 construction and application.

518 We introduced a new and more robust method for interpolation of L_x/T_x values onto the SGC. The new
519 sR (synthetic regenerative dose) method, reduces the influence of outliers in individual L_x/T_x on the
520 interpolation and D_e calculation. With the sR method a synthetic L_x/T_x, based on the growth curves of
521 the individual grain, is used for D_e calculations with the SGC method. Since the sR method relies on the
522 individual growth curves, no measurement time is saved. Therefore, we further tested how to reduce
523 regenerative cycles (rc) to obtain a suitable growth curve for the sR method. With our new established
524 rcsRxSGC method we were able to reduce our measurement time per disc by ~60 %. Furthermore, we
525 were able to calculate around twice as many D_e per disc with the rcsRxSGC method than with the SAR
526 procedure. Thus, potentially more measurement time can be saved, since fewer discs need to be
527 measured to gain a sufficient amount of suitable grains.

528 We investigated the relationship of K-content and luminescence characteristics, as well as their
529 implications for internal dose rate determination. Therefore, we measured the geochemical composition
530 of the grains previously analysed for their luminescence properties using a costly and time-consuming

531   scanning electron microscope (SEM) with energy-dispersive X-ray spectroscopy (EDX) attachment.

532   Since no correlation between the K-contents and luminescence properties could be found, we conclude

533   that for single grain measurements in feldspars with heterogeneous K-contents the internal dose rate

534   estimation should not be based on an average literature-based value. Further, we cannot recommend

535   using SEM-EDX measurements to overcome the problem, since they are costly and time consuming.

536   Therefore, the internal dose rate determination for single grain luminescence measurements remains a

537   challenge.

538   When dealing with geochemically heterogeneous feldspars which give few suitable luminescence

539   signals during single grain pIRIR measurements, we recommend using the rcsRxSGC method with a sR

540   in the size of the expected D_e and rc consisting of a recuperation point, a recycling point with a size

541   smaller than the expected D_e, and an additional dose point with a size of D_0 to $2D_0$ of the xSGC. Yet a

542   feasible solution for single grain K-content measurements is still needed.

543

544   **7. Glossary**

545   dataset A   dataset build with five samples from the Atacama Desert (cf. Tab. 1)

546   dataset X   dataset build with five samples from outside the Atacama Desert (cf. Tab. 1)

547   D_i regenerative dose

548   D_{r1} regenerative dose from which the L_x/T_x value is used for fitting onto the SGC

549   L_{sR} and T_{sR} synthetic L_{r1}/T_{r1} signal used for fitting onto the SGC

550   L_{r1} and T_{r1} signal and test dose signal used for fitting onto the SGC

551   rc   reduced measurement cycles

552   rcsRxSGC   SGC build with dataset X and data from A with reduced cycles and synthetic

553   regenerative dose used for fitting

554   r_s Spearman rank correlation coefficient

555   SGC   standardised growth curve

556   sR   synthetic regenerative dose

557   xSGC   SGC build with dataset X

558

559

Declaration of competing interest

563

Acknowledgements

580

References

Amundson, R., Richter, D.D., Humphreys, G.S., Jobbágy, E.G., Gaillardet, J., 2007. Coupling between Biota and Earth Materials in the Critical Zone. Elements 3, 327–332. https://doi.org/10.2113/gselements.3.5.327

Balian, H.G., Eddy, N.W., 1977. Figure-of-merit (FOM), an improved criterion over the normalized chi-squared test for assessing goodness-of-fit of gamma-ray spectral peaks. Nuclear Instruments and Methods 145, 389–395. https://doi.org/10.1016/0029-554X(77)90437-2

Bartz, M., Duval, M., Brill, D., Zander, A., King, G.E., Rhein, A., Walk, J., Stauch, G., Lehmkuhl, F., Brückner, H., 2020a. Testing the potential of K-feldspar pIR-IRSL and quartz ESR for dating coastal alluvial fan complexes in arid environments. Quaternary International, Electron spin resonance (ESR) dating in Quaternary studies: evolution, recent advances and applications 556, 124–143. https://doi.org/10.1016/j.quaint.2020.03.037

Bartz, M., Walk, J., Binnie, S.A., Brill, D., Stauch, G., Lehmkuhl, F., Hoffmeister, D., Brückner, H., 2020b. Late Pleistocene alluvial fan evolution along the coastal Atacama Desert (N Chile). Global and Planetary Change 190, 103091. https://doi.org/10.1016/j.gloplacha.2019.103091

596 Bonnet, S., Reimann, T., Wallinga, J., Lague, D., Davy, P., Lacoste, A., 2019. Landscape dynamics
597   revealed by luminescence signals of feldspars from fluvial terraces. Sci Rep 9, 8569.
598   https://doi.org/10.1038/s41598-019-44533-4

599 Brill, D., Reimann, T., Wallinga, J., May, S.M., Engel, M., Riedesel, S., Brückner, H., 2018. Testing the
600   accuracy of feldspar single grains to date late Holocene cyclone and tsunami deposits.
601   Quaternary Geochronology 48, 91–103. https://doi.org/10.1016/j.quageo.2018.09.001

602 Del Río, I., Sawakuchi, A.O., González, G., 2019. Luminescence dating of sediments from central
603   Atacama Desert, northern Chile. Quaternary Geochronology 53, 101002.
604   https://doi.org/10.1016/j.quageo.2019.05.001

605 Diederich, J.L., Wennrich, V., Bao, R., Büttner, C., Bolten, A., Brill, D., Buske, S., Campos, E.,
606   Fernández-Galego, E., Gödickmeier, P., Ninnemann, L., Reyers, M., Ritter, B., Ritterbach, L.,
607   Rolf, C., Scheidt, S., Dunai, T.J., Melles, M., 2020. A 68 ka precipitation record from the
608   hyperarid core of the Atacama Desert in northern Chile. Global and Planetary Change 184,
609   103054. https://doi.org/10.1016/j.gloplacha.2019.103054

610 Dietrich, W.E., Perron, J.T., 2006. The search for a topographic signature of life. Nature 439, 411–418.
611   https://doi.org/10.1038/nature04452

612 Finch, A.A., Klein, J., 1999. The causes and petrological significance of cathodoluminescence emissions
613   from alkali feldspars. Contrib Mineral Petrol 135, 234–243.
614   https://doi.org/10.1007/s004100050509

615 Fitzsimmons, K.E., Rhodes, E.J., Barrows, T.T., 2010. OSL dating of southeast Australian quartz: A
616   preliminary assessment of luminescence characteristics and behaviour. Quaternary
617   Geochronology, 12th International Conference on Luminescence and Electron Spin Resonance
618   Dating (LED 2008) 5, 91–95. https://doi.org/10.1016/j.quageo.2009.02.009

619 Fuchs, M., Owen, L.A., 2008. Luminescence dating of glacial and associated sediments: review,
620   recommendations and future directions. Boreas 37, 636–659. https://doi.org/10.1111/j.1502-
621   3885.2008.00052.x

622 Garcia-Guinea, J., Townsend, P.D., Sanchez-Muñoz, L., Rojo, J.M., 1999. Ultraviolet-blue ionic
623   luminescence of alkali feldspars from bulk and interfaces. Phys Chem Min 26, 658–667.
624   https://doi.org/10.1007/s002690050231

625 Geake, J.E., Walker, G., Mills, A.A., Garlick, G.F.J., 1972. Luminescence of lunar material excited by
626   electrons. Proceedings of the Lunar Science Conference 2971–2977.

627 Giardino, J.R., Houser, C., 2015. Principles and dynamics of the critical zone, Developments in earth
628   surface processes. Elsevier, Amsterdam Boston.

629 Guralnik, B., Jain, M., Herman, F., Ankjærgaard, C., Murray, A.S., Valla, P.G., Preusser, F., King, G.E.,
630   Chen, R., Lowick, S.E., Kook, M., Rhodes, E.J., 2015. OSL-thermochronometry of feldspar
631   from the KTB borehole, Germany. Earth and Planetary Science Letters 423, 232–243.
632   https://doi.org/10.1016/j.epsl.2015.04.032

633 Huntley, D.J., Baril, M.R., 1997. The K content of the K-feldspars being measured in optical dating or
634   in thermoluminescence dating. Ancient TL 15, 3.

635 Kars, R.H., Reimann, T., Wallinga, J., 2014. Are feldspar SAR protocols appropriate for post-IR IRSL
636   dating? Quaternary Geochronology 22, 126–136. https://doi.org/10.1016/j.quageo.2014.04.001

637 Kook, M.H., Murray, A.S., Lapp, T., Denby, P.H., Ankjærgaard, C., Thomsen, K., Jain, M., Choi, J.H.,
638   Kim, G.H., 2011. A portable luminescence dating instrument. Nuclear Instruments and Methods
639   in Physics Research Section B: Beam Interactions with Materials and Atoms 269, 1370–1378.
640   https://doi.org/10.1016/j.nimb.2011.03.014

641 Lambert, R., 2018. Investigating thermal decay in K-feldspar for the application of IRSL
642   thermochronometry on the Mont Blanc massif. University of Lausanne, Lausanne.

643 Lapp, T., Jain, M., Thomsen, K.J., Murray, A.S., Buylaert, J.-P., 2012. New luminescence measurement
644   facilities in retrospective dosimetry. Radiation Measurements 47, 803–808.
645   https://doi.org/10.1016/j.radmeas.2012.02.006

646 Li, B., Jacobs, Z., Roberts, R.G., 2016. Investigation of the applicability of standardised growth curves
647   for OSL dating of quartz from Haua Fteah cave, Libya. Quaternary Geochronology 35, 1–15.
648   https://doi.org/10.1016/j.quageo.2016.05.001

Li, B., Jacobs, Z., Roberts, R.G., Li, S.-H., 2018. Single-grain dating of potassium-rich feldspar grains: Towards a global standardised growth curve for the post-IR IRSL signal. Quaternary Geochronology 45, 23–36. https://doi.org/10.1016/j.quageo.2018.02.001

Li, B., Roberts, R.G., Jacobs, Z., Li, S.-H., 2015a. Potential of establishing a 'global standardised growth curve' (gSGC) for optical dating of quartz from sediments. Quaternary Geochronology 27, 94–104. https://doi.org/10.1016/j.quageo.2015.02.011

Li, B., Roberts, R.G., Jacobs, Z., Li, S.-H., Guo, Y.-J., 2015b. Construction of a 'global standardised growth curve' (gSGC) for infrared stimulated luminescence dating of K-feldspar. Quaternary Geochronology 27, 119–130. https://doi.org/10.1016/j.quageo.2015.02.010

Li, S.-H., Wintle, A.G., 1992. Luminescence sensitivity change due to bleaching of sediments. International Journal of Radiation Applications and Instrumentation. Part D. Nuclear Tracks and Radiation Measurements 20, 567–573. https://doi.org/10.1016/1359-0189(92)90006-H

Mahan, S.A., Rittenour, T.M., Nelson, M.S., Ataee, N., Brown, N., DeWitt, R., Durcan, J., Evans, M., Feathers, J., Frouin, M., Guérin, G., Heydari, M., Huot, S., Jain, M., Keen-Zebert, A., Li, B., López, G.I., Neudorf, C., Porat, N., Rodrigues, K., Sawakuchi, A.O., Spencer, J.Q.G., Thomsen, K., 2022. Guide for interpreting and reporting luminescence dating results. GSA Bulletin. https://doi.org/10.1130/B36404.1

May, S.M., Meine, L., Hoffmeister, D., Brill, D., Medialdea, A., Wennrich, V., Gröbner, M., Schulte, P., Steininger, F., Deprez, M., de Kock, T., Bubenzer, O., 2020. Origin and timing of past hillslope activity in the hyper-arid core of the Atacama Desert – The formation of fine sediment lobes along the Chuculay Fault System, Northern Chile. Global and Planetary Change 184, 103057. https://doi.org/10.1016/j.gloplacha.2019.103057

May, S.M., Zander, A., Francois, J.P., Kelletat, D., Pötsch, S., Rixhon, G., Brückner, H., 2015. Chronological and geoarchaeological investigations on an anthropogenic shell accumulation layer in the Longotoma dune field (Central Chile). Quaternary International 367, 32–41. https://doi.org/10.1016/j.quaint.2014.06.005

Mueller, D., Preusser, F., 2022. Investigating the applicability of a standardised growth curve approach on Middle Pleistocene sediments from northern Switzerland. Quaternary Geochronology 67, 101238. https://doi.org/10.1016/j.quageo.2021.101238

Murray, A.S., Wintle, A.G., Wallinga (INVITED), J., 2002. Dose Estimation Using Quartz OSL in the Non-linear Region of the Growth Curve. Radiation Protection Dosimetry 101, 371–374. https://doi.org/10.1093/oxfordjournals.rpd.a006004

Oeser, R.A., Stroncik, N., Moskwa, L.-M., Bernhard, N., Schaller, M., Canessa, R., van den Brink, L., Köster, M., Brucker, E., Stock, S., Fuentes, J.P., Godoy, R., Matus, F.J., Oses Pedraza, R., Osses McIntyre, P., Paulino, L., Seguel, O., Bader, M.Y., Boy, J., Dippold, M.A., Ehlers, T.A., Kühn, P., Kuzyakov, Y., Leinweber, P., Scholten, T., Spielvogel, S., Spohn, M., Übernickel, K., Tielbörger, K., Wagner, D., von Blanckenburg, F., 2018. Chemistry and microbiology of the Critical Zone along a steep climate and vegetation gradient in the Chilean Coastal Cordillera. CATENA 170, 183–203. https://doi.org/10.1016/j.catena.2018.06.002

O'Gorman, K., Tanner, D., Sontag-González, M., Li, B., Brink, F., Jones, B.G., Dosseto, A., Jatmiko, Roberts, R.G., Jacobs, Z., 2021. Composite grains from volcanic terranes: Internal dose rates of supposed 'potassium-rich' feldspar grains used for optical dating at Liang Bua, Indonesia. Quaternary Geochronology 64, 101182. https://doi.org/10.1016/j.quageo.2021.101182

Peng, J., Li, B., 2017. Single-aliquot Regenerative-Dose (SAR) and Standardised Growth Curve (SGC) Equivalent Dose Determination in a Batch Model Using the R Package 'numOSL' 35.

Peng, J., Li, B., More, J., Garbow, B., Hillstrom, K., Burkardt, J., Gilbert, P., Varadhan, R., 2018. numOSL: Numeric Routines for Optically Stimulated Luminescence Dating.

Prescott, J.R., Fox, P.J., 1993. Three-dimensional thermoluminescence spectra of feldspars. J. Phys. D: Appl. Phys. 26, 2245–2254. https://doi.org/10.1088/0022-3727/26/12/024

Reimann, T., Román-Sánchez, A., Vanwalleghem, T., Wallinga, J., 2017. Getting a grip on soil reworking – Single-grain feldspar luminescence as a novel tool to quantify soil reworking rates. Quaternary Geochronology 42, 1–14. https://doi.org/10.1016/j.quageo.2017.07.002

Riedesel, S., Bell, A.M.T., Duller, G.A.T., Finch, A.A., Jain, M., King, G.E., Pearce, N.J., Roberts, H.M., 2021. Exploring sources of variation in thermoluminescence emissions and anomalous

703   fading   in   alkali   feldspars.   Radiation   Measurements   141,   106541.
704   https://doi.org/10.1016/j.radmeas.2021.106541
705   Riedesel, S., King, G.E., Prasad, A.K., Kumar, R., Finch, A.A., Jain, M., 2019. Optical determination
706   of the width of the band-tail states, and the excited and ground state energies of the principal
707   dosimetric   trap   in   feldspar.   Radiation   Measurements   125,   40–51.
708   https://doi.org/10.1016/j.radmeas.2018.08.019
709   Ritter, B., Wennrich, V., Medialdea, A., Brill, D., King, G., Schneiderwind, S., Niemann, K., Fernández-
710   Galego, E., Diederich, J., Rolf, C., Bao, R., Melles, M., Dunai, T.J., 2019. "Climatic fluctuations
711   in the hyperarid core of the Atacama Desert during the past 215 ka." Sci Rep 9, 5270.
712   https://doi.org/10.1038/s41598-019-41743-8
713   Román-Sánchez, A., Laguna, A., Reimann, T., Giráldez, J.V., Peña, A., Vanwalleghem, T., 2019a.
714   Bioturbation and erosion rates along the soil-hillslope conveyor belt, part 2: Quantification
715   using an analytical solution of the diffusion–advection equation. Earth Surface Processes and
716   Landforms 44, 2066–2080. https://doi.org/10.1002/esp.4626
717   Román-Sánchez, A., Reimann, T., Wallinga, J., Vanwalleghem, T., 2019b. Bioturbation and erosion
718   rates along the soil-hillslope conveyor belt, part 1: Insights from single-grain feldspar
719   luminescence.   Earth   Surface   Processes   and   Landforms   44,   2051–2065.
720   https://doi.org/10.1002/esp.4628
721   Sawakuchi, A.O., Blair, M.W., DeWitt, R., Faleiros, F.M., Hyppolito, T., Guedes, C.C.F., 2011.
722   Thermal history versus sedimentary history: OSL sensitivity of quartz grains extracted from
723   rocks   and   sediments.   Quaternary   Geochronology   6,   261–272.
724   https://doi.org/10.1016/j.quageo.2010.11.002
725   Smedley, R.K., Duller, G.A.T., Pearce, N.J.G., Roberts, H.M., 2012. Determining the K-content of
726   single-grains of feldspar for luminescence dating. Radiation Measurements, Proceedings of the
727   13th International Conference on Luminescence and Electron Spin Resonance Dating, 10–14
728   July, 2011, Toruń, Poland 47, 790–796. https://doi.org/10.1016/j.radmeas.2012.01.014
729   Sontag-González, M., Li, B., O'Gorman, K., Sutikna, T., Jatmiko, Jacobs, Z., Roberts, R.G., 2021.
730   Establishing a pIRIR procedure for De determination of composite mineral grains from volcanic
731   terranes: A case study of sediments from Liang Bua, Indonesia. Quaternary Geochronology 65,
732   101181. https://doi.org/10.1016/j.quageo.2021.101181
733   Spearman, C., 1904. The proof and measurement of association between two things. The American
734   Journal of Psychology 15, 72–101. https://doi.org/10.2307/1412159
735   Spooner, N.A., 1992. Optical dating: Preliminary results on the anomalous fading of luminescence from
736   feldspars. Quaternary Science Reviews, Proceedings of the 6th International Specialist Seminar
737   on   Thermoluminescence   and   Electron   Spin   Resonance   Dating   11,   139–145.
738   https://doi.org/10.1016/0277-3791(92)90055-D
739   Starke, J., Ehlers, T.A., Schaller, M., 2020. Latitudinal effect of vegetation on erosion rates identified
740   along   western   South   America.   Science   367,   1358–1361.
741   https://doi.org/10.1126/science.aaz0840
742   Steffen, D., Preusser, F., Schlunegger, F., 2009. OSL quartz age underestimation due to unstable signal
743   components.   Quaternary   Geochronology   4,   353–362.
744   https://doi.org/10.1016/j.quageo.2009.05.015
745   Tchakerian, V., Pease, P., 2015. Chapter 14 - The Critical Zone in Desert Environments, in: Giardino,
746   J.R., Houser, C. (Eds.), Developments in Earth Surface Processes. Elsevier, pp. 449–472.
747   https://doi.org/10.1016/B978-0-444-63369-9.00014-8
748   Thomsen, K.J., Murray, A.S., Jain, M., Bøtter-Jensen, L., 2008. Laboratory fading rates of various
749   luminescence signals from feldspar-rich sediment extracts. Radiation Measurements 43, 1474–
750   1486. https://doi.org/10.1016/j.radmeas.2008.06.002
751   Tokuyasu, K., Tanaka, K., Tsukamoto, S., Murray, A., 2010. The Characteristics of OSL Signal from
752   Quartz Grains Extracted from Modern Sediments in Japan.
753   Veit, H., Preusser, F., Trauerstein, M., 2015. The Southern Westerlies in Central Chile during the two
754   last glacial cycles as documented by coastal aeolian sand deposits and intercalating palaeosols.
755   CATENA 134, 30–40. https://doi.org/10.1016/j.catena.2014.11.002
756   Wei, T., Simko, V., 2023. R package "corrplot": Visualization of a Correlation Matrix. (Version 0.92),.

757   Zinelabedin, A., Riedesel, S., Reimann, T., Ritter, B., Dunai, T.J., 2022. Testing the potential of using
758   coarse-grain feldspars for post-IR IRSL dating of calcium sulphate-wedge growth in the
759   Atacama   Desert.   Quaternary   Geochronology   101341.
760   https://doi.org/10.1016/j.quageo.2022.101341

761 <div align="center">**Supplementary Material**</div>

762
763 <div align="center">**Testing the applicability of standardised growth curves (SGC) for chemically heterogeneous single-grain feldspars from the Atacama Desert, Chile**</div>

764 Linda A.E. Maßon[1*], Svenja Riedesel[1,2], Anja Zander[1], Mariana Sontag-González[3,4], Tony
765 Reimann[1]

766 [1] Institute of Geography, University of Cologne, Germany
767 [2] Radiation Physics Division, Department of Physics, Technical University of Denmark, Denmark
768 [3] Institute of Geography, Justus-Liebig-University Gießen, Germany
769 [4] Department of Geosciences, Stony Brook University, NY 11794-2100, USA
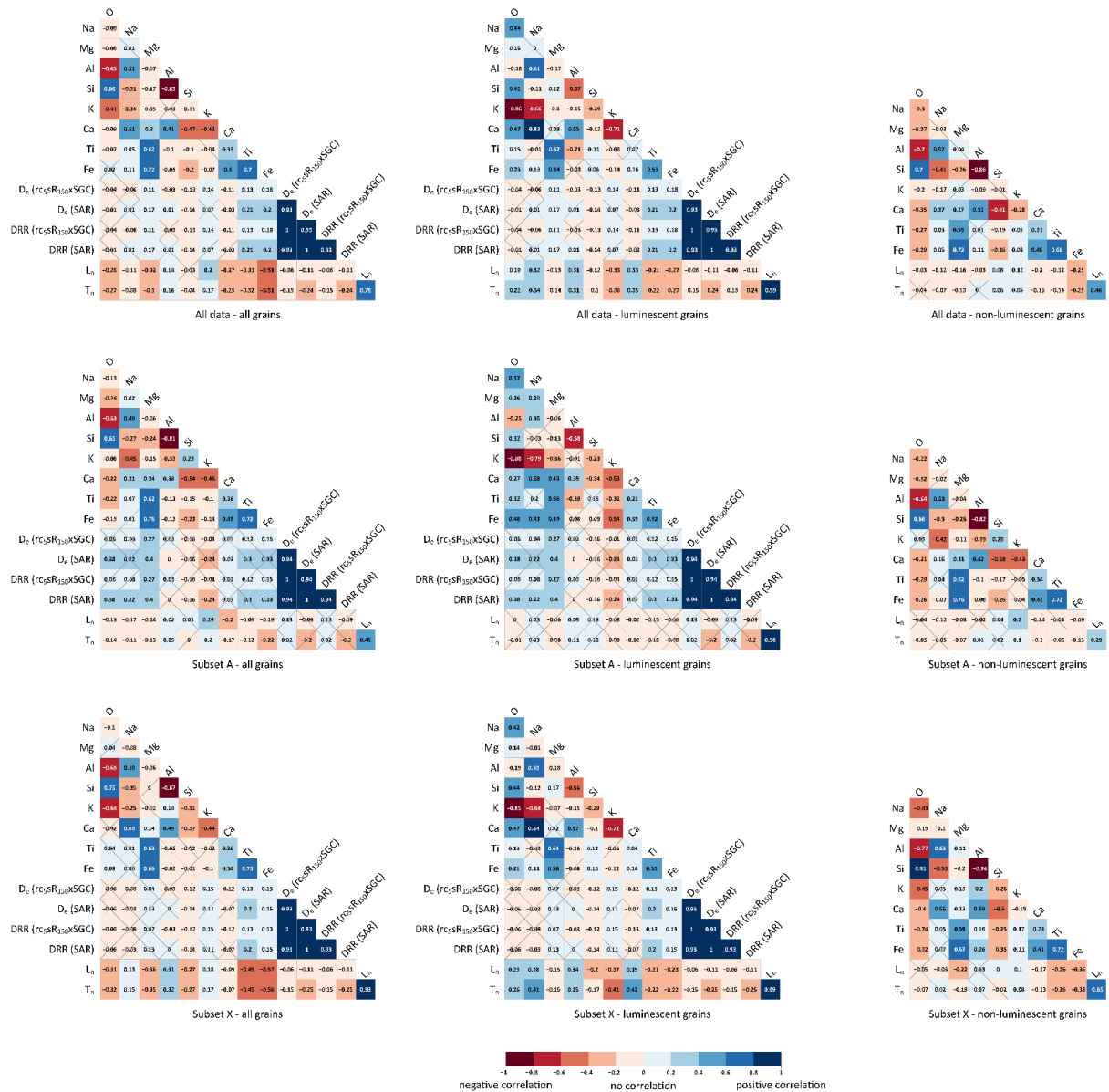
770

771 *Fig. S1: correlation matrices of the complete dataset (subset A + X) in the first row, subset A in the second row and subset X*
772 *in the third row, for all grains in the first column, luminescent grains in the second column and non-luminescent grains in the*
773 *third column. Numbers in the squares represent Spearman's rank correlation coefficient values and their colour the strength*
774 *of the correlation. For not significant correlations with a p-value above 0.05 % the squares are x-ed out.*

775 *Table S1: summary of grain rejection for all ten samples for the SAR procedure, the SGC method (samples 1-5) and he xSGC method (samples 6-10) for the full data sets using all SAR cycles.*

776

Description	ARO-18-08-LP	CSA-1-2-2	LAGU-1-1	PAG-6-4b	PAG-6-6b	ABLR-1	HAM-5	ISM-7	KTB-383-C	MBT-I-2430
Total number of analysed grains	500	500	500	500	500	500	500	500	500	500
Rejection criterion: Tn below 3 σ BG	385	421	268	433	416	314	173	360	62	3
Rejection criterion: RSE of Tn exceeds 25 %	75	52	67	58	52	104	65	74	29	4
Rejection criterion: recycling ratio 1 outsides [0.9:1.1]	3	1	9	1	2	8	13	2	43	52
Rejection criterion: recycling ratio 2 outsides [0.9:1.1]	0	0	0	0	0	0	0	0	0	0
Rejection criterion: recycling ratio 3 outsides [0.9:1.1]	0	0	0	0	0	0	0	0	0	0
Rejection criterion: recuperation 1 exceeds 10 %	0	0	0	0	1	1	1	0	6	0
Rejection criterion: recuperation 2 exceeds 10 %	0	0	0	0	0	0	0	0	0	0
Function fitGrowth(): improper input argument	0	0	0	0	0	0	0	0	0	0
Function fitGrowth(): failed in growth curve fitting	0	0	0	1	0	3	0	0	1	0
Rejection criterion: FOM of growth curve exceeds 10%	23	22	90	6	11	41	65	31	62	74
Rejection criterion: RCS of growth curve exceeds 10	1	0	4	0	10	5	75	1	201	58
Total number of rejected grains	487	496	438	499	492	476	392	468	404	191
Total number of accepted grains	13	4	62	1	8	24	108	32	96	309

777 *Table S2: summary of the results for dataset A using the sRxSGC approach, in relation to the De calculated with the SAR approach and to a dose recovery ratio (DRR) of 1.*

synthetic regenerative dose (sR) size used in the sRxSGC approach	50	100	125	150	175	200	300	800
n D_e	88	88	88	88	88	88	88	88
n D_e common grains sRxSGC & SAR	86	86	86	86	86	86	86	87
In unity within 10 %	69	83	86	85	76	69	36	11
In unity within 1 σ	16	3	0	1	10	16	36	24
In unity within 2 σ	1	0	0	0	0	1	12	28
Not in unity	0	0	0	0	0	0	2	24
NA in either sRxSGC or SAR	2	2	2	2	2	2	2	1
Differences in D_e								
Min	0.37	0.00	0.00	0.03	0.01	0.02	0.07	1.58
Max	46.63	25.10	19.31	16.53	25.31	34.31	87.21	282.54
Mean	9.36	3.86	2.42	2.65	4.81	7.48	19.61	59.99
sd	9.84	4.96	3.16	3.10	4.74	7.00	16.42	50.05
CV	1.05	1.29	1.31	1.17	0.99	0.94	0.84	0.83
DRR (all grains)								
DRR between 0.9-1.1	25	20	26	30	30	33	29	15
DRR with 1 σ error between 0.9-1.1	28	35	31	26	30	28	34	20
DRR with 1 σ error not between 0.9-1.1	33	31	29	30	26	25	23	52
NA in either	2	2	2	2	2	2	2	1
Mean DRR	0.87	0.86	0.87	0.89	0.9	0.91	0.98	1.19
DRR (common grains)								
DRR between 0.9-1.1	25	20	26	30	30	33	29	15
DRR with 1 σ error between 0.9-1.1	28	35	31	26	30	28	34	20
DRR with 1 σ error not between 0.9-1.1	33	31	29	30	26	25	23	52
NA in either	2	2	2	2	2	2	2	1
Mean DRR	0.87	0.86	0.87	0.89	0.9	0.91	0.98	1.19
Correlation with SAR (r_s values)	0.9	0.99	0.99	0.99	0.97	0.94	0.76	0.21

778 *Table S3: summary of grain rejection for all ten samples for the SAR procedure, the SGC method (samples 1-5) and he xSGC method (samples 6-10) for reduced dataset using the cycles of rc5.*

Description	ARO-18-08-LP	CSA-1-2-2	LAGU-1-1	PAG-6-4b	PAG-6-6b	ABLR-1	HAM-5	ISM-7	KTB-383-C	MBT-I-2430
Total number of analysed aliquots (grains)	500	500	500	500	500	500	500	500	500	500
Rejection criterion: Tn below 3 sigma BG	385	421	268	433	416	314	173	360	62	3
Rejection criterion: RSE of Tn exceeds 25%	75	52	67	58	52	104	65	74	29	4
Rejection criterion: recycling ratio 1 outsides [0.9:1.1]	3	1	9	1	2	8	13	2	43	52
Rejection criterion: recycling ratio 2 outsides [0.9:1.1]	0	0	0	0	0	0	0	0	0	0
Rejection criterion: recycling ratio 3 outsides [0.9:1.1]	0	0	0	0	0	0	0	0	0	0
Rejection criterion: recuperation 1 exceeds 10%	0	0	0	0	1	1	1	0	6	0
Rejection criterion: recuperation 2 exceeds 10%	0	0	0	0	1	0	0	0	0	0
Function fitGrowth(): improper input argument	0	0	0	0	0	0	0	0	0	0
Function fitGrowth(): failed in growth curve fitting	0	0	0	1	0	2	0	0	0	0
Rejection criterion: FOM of growth curve exceeds 10%	7	9	12	1	2	11	9	5	3	4
Rejection criterion: RCS of growth curve exceeds 10	0	0	0	0	1	0	7	1	27	7
Total number of rejected aliquots (grains)	470	483	356	494	475	440	268	442	170	70
Total number of accepted aliquots (grains)	30	17	144	6	25	60	232	58	330	430

779

780 *Table S4: summary of the results for dataset A using the rcsR150xSGC approach, in relation to the De calculated with the SAR approach and to a dose recovery ratio (DRR) of 1. Headers indicating the size*
781 *of the dose (Di) of the used cycles, with the first 150 being the "natural" cycle. The abbreviations refer to Table 3.*

Reduced cycles used (sR = 150 Gy)	150-0-50-300	150-0-50-500	150-0-50-800	150-0-50-150-50	150-0-50-300-50	150-0-50-500-50	150-0-50-800-50	150-0-150-300-150	150-0-150-500-150	150-0-150-800-150
Abbreviation	rc_1	rc_2	rc_3	rc_4	rc_5	rc_6	rc_7	rc_8	rc_9	rc_{10}
n D_e	219	226	229	142	198	206	212	186	200	208
n D_e common grains rcsR$_{150}$xSGC & SAR	86	86	87	59	86	86	87	85	86	86
In unity within 10 %	68	53	48	41	72	69	64	62	63	63
In unity within 1 σ	18	33	38	18	14	17	22	22	22	22
In unity within 2 σ	0	0	1	0	0	0	1	1	1	1
Not in unity	0	0	0	0	0	0	0	0	0	0
NA in either rcsR$_{150}$xSGC or SAR	158	159	155	125	130	132	134	120	129	133
Differences in D$_e$										
Min	0.11	0.10	0.48	0.15	0.03	0.17	0.43	0.22	0.21	0.21
Max	45.08	92.96	163.44	38.78	29.37	66.85	72.05	33.63	33.63	33.63
Mean	9.00	12.21	15.33	8.70	7.40	8.74	11.43	9.98	9.85	9.85
sd	8.25	12.93	19.67	8.02	6.51	9.45	10.45	7.57	7.61	7.61
CV	0.92	1.06	1.28	0.92	0.88	1.08	0.91	0.76	0.77	0.77
DRR (all grains)										
DRR between 0.9-1.1	58	50	46	25	54	57	47	59	65	66
DRR with 1 σ error between 0.9-1.1	85	82	73	36	80	66	66	63	68	71
DRR with 1 σ error not between 0.9-1.1	75	93	110	53	63	82	99	62	66	67
NA in either	26	20	13	70	19	13	9	21	16	12
Mean DRR	0.91	0.88	0.88	0.78	0.9	0.89	0.87	0.95	0.98	0.99
DRR (common grains)										
DRR between 0.9-1.1	21	18	17	13	23	24	21	32	32	32
DRR with 1 σ error between 0.9-1.1	34	28	25	17	33	22	18	26	26	26
DRR with 1 σ error not between 0.9-1.1	31	40	45	29	30	40	48	27	28	28
NA in either	26	20	13	70	19	13	9	21	16	12
Mean DRR	0.88	0.87	0.86	0.79	0.87	0.85	0.84	0.91	0.9	0.9
Correlation with SAR (r_s values)	0.92	0.9	0.9	0.84	0.94	0.94	0.95	0.89	0.89	0.89

782
783 *Table S5: summary of the SEM-EDX measurement results for the nine elements measured. For each element the results are given for subset A, subset X and the complete dataset. The table is further divided in all grains (upper third), luminescent grains (middle third) and the non-luminescent grains (bottom third).*

All

Element	O subset A	O subset X	O total	Na subset A	Na subset X	Na total	Mg subset A	Mg subset X	Mg total	Al subset A	Al subset X	Al total	Si subset A	Si subset X	Si total	K subset A	K subset X	K total	Ca subset A	Ca subset X	Ca total	Ti subset A	Ti subset X	Ti total	Fe subset A	Fe subset X	Fe total
n measurements	1193	1135	2328	1193	1135	2328	1193	1135	2328	1193	1135	2328	1193	1135	2328	1193	1135	2328	1193	1135	2328	1193	1135	2328	1193	1135	2328
n (without 0)	1193	1135	2328	1158	978	2136	531	258	789	1185	1067	2252	1193	1135	2328	1152	1002	2154	1046	658	1704	519	325	844	1071	562	1633
Min	44.04	42.55	42.55	0	0	0	0	0	0	0	0	0	12.22	18.63	12.22	0	0	0	0	0	0	0	0	0	0	0	0
Min (without 0)	44.04	42.55	42.55	0.32	0.13	0.13	0.07	0.08	0.07	0.34	0.25	0.25	12.22	18.63	12.22	0.06	0.06	0.06	0.07	0.03	0.03	0.04	0.04	0.04	0.08	0.07	0.07
Max	55.37	56.25	56.25	8.51	9.02	9.02	15.00	6.68	15.00	30.93	23.84	30.93	48.19	49.02	49.02	13.98	14.68	14.68	11.97	13.27	13.27	3.22	4.71	4.71	8.57	17.69	17.69
Mean	48.02	47.70	47.87	3.33	2.65	3.00	0.39	0.14	0.26	9.33	8.54	8.94	32.29	34.94	33.58	3.40	4.21	3.80	1.80	1.09	1.45	0.16	0.13	0.15	1.28	0.60	0.95
sd	1.74	2.25	2.01	1.84	2.35	2.13	0.78	0.39	0.63	2.73	3.95	3.40	3.72	5.99	5.13	3.01	4.88	4.05	2.18	1.83	2.05	0.26	0.32	0.29	1.39	1.44	1.46
Coefficient of variation	0.04	0.05	0.04	0.55	0.89	0.71	2.01	2.90	2.40	0.29	0.46	0.38	0.12	0.17	0.15	0.89	1.16	1.07	1.21	1.68	1.41	1.61	2.42	1.97	1.08	2.42	1.53

luminescent

Element	O subset A	O subset X	O total	Na subset A	Na subset X	Na total	Mg subset A	Mg subset X	Mg total	Al subset A	Al subset X	Al total	Si subset A	Si subset X	Si total	K subset A	K subset X	K total	Ca subset A	Ca subset X	Ca total	Ti subset A	Ti subset X	Ti total	Fe subset A	Fe subset X	Fe total
n measurements	65	434	499	65	434	499	65	434	499	65	434	499	65	434	499	65	434	499	65	434	499	65	434	499	65	434	499
n (without 0)	65	434	499	65	402	467	6	29	35	65	420	485	65	434	499	65	410	475	36	209	245	6	28	34	37	88	125
Min	44.88	43.86	43.86	0.42	0	0	0	0	0	1.65	0	0.00	27.66	28.02	27.66	0.24	0	0	0	0	0	0	0	0	0	0	0
Min (without 0)	44.88	43.86	43.86	0.42	0.13	0.13	0.22	0.12	0.12	1.65	0.59	0.59	27.66	28.02	27.66	0.24	0.06	0.06	0.27	0.07	0.07	0.04	0.04	0.04	0.09	0.08	0.08
Max	52.53	54.42	54.42	7.7	9.015	9.015	1.67	2.31	2.31	17.05	14.44	17.05	44.23	48.72	48.72	13.33	14.63	14.63	4.42	5.46	5.46	1.13	1.34	1.34	2.45	8.81	8.81
Mean	46.5	46.63	46.62	2.44	2.87	2.82	0.06	0.03	0.03	9.91	9.74	9.76	31.86	33.03	32.88	8.38	6.84	7.04	0.48	0.73	0.69	0.04	0.02	0.02	0.28	0.11	0.13
sd	1.48	1.95	1.89	1.64	2.66	2.55	0.26	0.15	0.17	1.95	2.99	2.87	2.58	4.48	4.30	3.97	5.81	5.62	0.79	1.06	1.03	0.16	0.12	0.13	0.51	0.51	0.51
Coefficient of variation	0.03	0.04	0.04	0.67	0.93	0.91	3.94	5.66	5.32	0.20	0.31	0.29	0.08	0.14	0.13	0.47	0.85	0.80	1.63	1.47	1.49	3.84	5.46	5.13	1.82	4.72	3.93

non-luminescent

Element	O subset A	O subset X	O total	Na subset A	Na subset X	Na total	Mg subset A	Mg subset X	Mg total	Al subset A	Al subset X	Al total	Si subset A	Si subset X	Si total	K subset A	K subset X	K total	Ca subset A	Ca subset X	Ca total	Ti subset A	Ti subset X	Ti total	Fe subset A	Fe subset X	Fe total
n measurements	1128	701	1829	1128	701	1829	1128	701	1829	1128	701	1829	1128	701	1829	1128	701	1829	1128	701	1829	1128	701	1829	1128	701	1829
n (without 0)	1128	701	1829	1093	576	1669	525	229	754	1120	647	1767	1128	701	1829	1087	592	1679	1010	449	1459	513	297	810	1034	474	1508
Min	44.04	42.55	42.55	0	0	0	0	0	0	0	0	0	12.22	18.63	12.22	0	0	0	0	0	0	0	0	0	0	0	0
Min (without 0)	44.04	42.55	42.55	0.32	0.15	0.15	0.07	0.08	0.07	0.34	0.25	0.25	12.22	18.63	12.22	0.06	0.10	0.06	0.07	0.03	0.03	0.04	0.04	0.04	0.08	0.07	0.07
Max	55.37	56.25	56.25	8.51	8.46	8.51	15	6.68	15	30.925	23.84	30.925	48.19	49.02	49.02	13.975	14.68	14.68	11.97	13.27	13.27	3.22	4.71	4.71	8.57	17.69	17.69
Mean	48.1	48.37	48.21	3.39	2.51	3.05	0.40	0.20	0.33	9.29	7.79	8.72	32.31	36.12	33.77	3.11	2.59	2.91	1.87	1.32	1.66	0.17	0.20	0.18	1.34	0.90	1.17
sd	1.71	2.17	1.91	1.84	2.12	2.00	0.79	0.47	0.69	2.76	4.27	3.50	3.78	6.48	5.32	2.68	3.27	2.93	2.21	2.15	2.20	0.26	0.38	0.31	1.40	1.73	1.55
Coefficient of variation	0.04	0.04	0.04	0.54	0.85	0.66	1.96	2.33	2.12	0.30	0.55	0.40	0.12	0.18	0.16	0.86	1.26	1.01	1.18	1.63	1.33	1.56	1.89	1.73	1.04	1.92	1.32

784